



## Ground-based Ku-band microwave observations of ozone in the polar middle atmosphere

David A. Newnham<sup>1</sup>, Mark A. Clilverd<sup>1</sup>, William D. J. Clark<sup>1</sup>, Michael Kosch,<sup>2,3,4</sup> Pekka T. Verronen,<sup>5,6</sup> and Alan E. E. Rogers<sup>7</sup>

5 <sup>1</sup>British Antarctic Survey, High Cross, Madingley Road, Cambridge, CB3 0ET, United Kingdom.

<sup>2</sup>Physics Department, Lancaster University, Lancaster, LA1 4YB, UK.

<sup>3</sup>South African National Space Agency (SANSA), Hospital Street, Hermanus 7200, South Africa.

<sup>4</sup>Department of Physics and Astronomy, University of the Western Cape, Robert Sobukwe Road, Bellville, 7535, South Africa.

<sup>5</sup>Sodankylä Geophysical Observatory, University of Oulu, Tähteläntie 62, 99600 Sodankylä, Finland.

10 <sup>6</sup>Space and Earth Observation Centre, Finnish Meteorological Institute, P.O. Box 503, 00101, Helsinki, Finland.

<sup>7</sup>MIT Haystack Observatory, Route 40, Westford, MA 01886, United States.

*Correspondence to:* David A. Newnham (dawn@bas.ac.uk)

**Abstract.** Ground-based observations of 11.072 GHz atmospheric ozone (O<sub>3</sub>) emission have been made using the Ny-Ålesund Ozone in the Mesosphere Instrument (NAOMI) at the UK Arctic Research Station (latitude 78°55'0" N, longitude 11°55'59" E), Spitsbergen. Seasonally-averaged O<sub>3</sub> vertical profiles in the Arctic polar mesosphere-lower thermosphere region for night-time and twilight conditions in the period 15 August 2017 to 15 March 2020 have been retrieved over the altitude range 62–98 km. NAOMI measurements are compared with corresponding, overlapping observations by the Sounding of the Atmosphere using Broadband Emission Radiometry (SABER) satellite instrument. The NAOMI and SABER data are binned according to the SABER instrument 60-day yaw cycles into 3-month ‘winter’ (15 December–15 March), ‘autumn’ (15 August–15 November), and ‘summer’ (15 April–15 July) periods. The NAOMI observations show the same year-to-year and seasonal variabilities as the SABER 9.6 μm O<sub>3</sub> data. The winter night-time (solar zenith angle, SZA ≥ 110°) and twilight (75° ≤ SZA ≤ 110°) NAOMI and SABER 9.6 μm O<sub>3</sub> volume mixing ratio (VMR) profiles agree to within the measurement uncertainties. However, for autumn twilight conditions the SABER 9.6 μm O<sub>3</sub> secondary maximum VMR values are higher than NAOMI over altitudes 88–97 km by 47% and 59% respectively in 2017 and 2018. Comparing the two SABER channels which measure O<sub>3</sub> at different wavelengths and use different processing schemes, the 9.6 μm O<sub>3</sub> autumn twilight VMR data for the three years 2017–19 are higher than the corresponding 1.27 μm measurements with the largest difference (58%) in the 65–95 km altitude range similar to the NAOMI observation. The SABER 9.6 μm O<sub>3</sub> summer daytime (SZA < 75°) mesospheric O<sub>3</sub> VMR is also consistently higher than the 1.27 μm measurement, confirming previously reported differences between the SABER 9.6 μm channel and measurements of mesospheric O<sub>3</sub> by other satellite instruments.

15  
20  
25



## 30 1 Introduction

### 1.1 Background information

Ozone ( $O_3$ ) is an important trace species in the mesosphere and lower thermosphere, affecting atmospheric heating rates and the chemical and radiative budgets of the middle atmosphere (Brasseur & Solomon, 2005; Sinnhuber et al., 2012; Palmroth et al., 2021). The secondary  $O_3$  maximum (Hays and Roble, 1973) near the mesopause at ~90–95 km arises from downward  
35 transport and recombination of atomic oxygen (O) produced by far-UV (FUV) dissociation of molecular oxygen ( $O_2$ ) in the lower thermosphere. The diurnal cycle in odd oxygen ( $O_x$ ) leads to rapid interconversion at twilight between daytime O and  $O_3$  at night. In the summer mesosphere, the abundance of odd hydrogen ( $HO_x$ ) from FUV photo-dissociation of water vapour leads to a deep minimum in  $O_3$  abundance. However, a seasonal tertiary  $O_3$  layer forms at altitudes ~70–75 km in mid- to high latitudes when  $H_2O$  is no longer efficiently dissociated into  $HO_x$  due to high optical depths in the FUV (Marsh et al., 2001).  
40 The tertiary  $O_3$  peak in the middle mesosphere is observed from early autumn until late spring between 30° latitude and the equatorward edge of the polar-night terminator (Hartogh et al., 2004). The spatial and temporal structure of the tertiary  $O_3$  layer in the polar winter mesosphere, and its night-time variability, has been reported (Smith et al., 2015, 2018; Sofieva et al., 2009). Mesospheric  $O_3$  is also strongly affected by space weather processes which increase energetic particle precipitation (EPP) into the atmosphere (Baker et al., 2018). D-region ionisation due to EPP increases mesospheric  $HO_x$  and odd nitrogen  
45 ( $NO_x$ ) which impact on  $O_3$  abundances (e.g., Daae et al., 2012; Andersson et al., 2014; Verronen & Lehmann, 2015; Zawedde et al., 2018). Atmospheric dynamical processes including meridional circulation, vertical diffusion, planetary and gravity wave activity, atmospheric tides, polar mesospheric cloud occurrences, and sudden stratospheric warming events also modify  $O_3$  distributions in the middle atmosphere (e.g., Pancheva et al., 2014; Limpasuvan et al., 2016; Siskind et al., 2018; Smith-Johnsen et al., 2018).

### 50 1.2 Previous ozone measurements

$O_3$  vertical profiles in the upper mesosphere (70–100 km) from observations by nine satellite instruments have been reviewed and compared by Smith et al. (2013). More recently,  $O_3$  profiles have been reported up to ~105 km during dark conditions and ~95 km during sunlit periods from measurements using the middle atmosphere modes of the Michelson Interferometer for Passive Atmospheric Sounding (MIPAS). Validation of the 10-year satellite dataset (López-Puertas et al., 2018) shows that  
55 MIPAS  $O_3$  has a positive bias of ~10% at 50–75 km and agrees with other instruments over 75–90 km to within 10% at night-time and 10–20% for daytime. Above 90 km, MIPAS daytime  $O_3$  agrees with other instruments to 10% but at night the positive bias increases from 10% at 90 km to 20% at 95–100 km. Daytime mesospheric  $O_3$  profiles derived from OSIRIS Infrared Imager observations of the 1.27  $\mu m$  oxygen airglow band were found to have positive biases of up to 25% below 75 km and up to 50% at higher altitudes, compared to other instruments on the Odin satellite (Li et al., 2020).  
60  $O_3$  vertical profiles are derived from the Sounding of the Atmosphere using Broadband Emission Radiometry (SABER) infrared 9.6  $\mu m$  emission and 1.27  $\mu m$  daytime airglow channels. However, daytime  $O_3$  VMR from SABER 9.6  $\mu m$



measurements is ~20–50% higher than other satellite instruments over the altitude range 60–80 km although night-time observations show better agreement with <10% difference (Smith et al., 2013). Applying updated, lower night-time atomic O values to the SABER processing scheme confirms that SABER 9.6  $\mu\text{m}$  daytime  $\text{O}_3$  is too large, with implications for inferred atomic hydrogen abundances (Mlynczak et al., 2018; Kulikov et al., 2019).

Ground-based millimetre-wave (mm-wave) radiometry in the 110–250 GHz frequency range provides continuous measurements of  $\text{O}_3$  (e.g., Hartogh et al., 2004; Daae et al., 2014; Ryan et al., 2016) over the altitude range ~20–75 km. Ground-based mm-wave measurements are of limited vertical resolution, typically ~8 km at best, but can be compared with more highly resolved  $\text{O}_3$  profiles from overlapping balloon-borne ozonesonde observations and satellite measurements by considering the retrieval diagnostics (Ryan et al., 2016). At lower, microwave frequencies the  $4_{0,4} \rightarrow 3_{1,3}$  rotational transition of  $^{16}\text{O}_3$  (using the notation  $J'_{K'_a, K'_c} \rightarrow J''_{K''_a, K''_c}$  where  $J'$ ,  $K'_a$ , and  $K'_c$  are the upper state rotational quantum numbers and  $J''$ ,  $K''_a$ , and  $K''_c$  are the lower state rotational quantum numbers) gives rise to a weak atmospheric line centred at 11.072 GHz. The emission line is within the 10.70–12.75 GHz frequency range of Ku-band downlinks used for direct broadcast satellite services in Europe. This has allowed ground-based microwave radiometers operating at 11.072 GHz to be developed using commercially-available Ku-band low noise block (LNB) downconverters developed for satellite receivers (Rogers et al., 2009; Tenneti et al., 2009). The atmosphere in the Ku-band (12–18 GHz) region is much less opaque than at 110–250 GHz and Doppler broadening for the 11.072 GHz line is 10–23 times smaller, allowing  $\text{O}_3$  to be retrieved at altitudes above 75 km including the secondary  $\text{O}_3$  layer (Newnham et al., 2019). Low-cost radiometer instruments have been constructed and operated as part of “The Mesospheric Ozone System for Atmospheric Investigations in the Classroom” (MOSAIC) educational project.  $\text{O}_3$  partial columns for the lower mesosphere (~50–80 km) and the upper mesosphere / lower thermosphere (~80–100 km) have been determined using MOSAIC observations from mid-latitude sites and used to estimate seasonal  $\text{O}_3$  variability near the mesopause (Rogers et al., 2012).

### 1.3 This work

In this work we report new, ground-based 11.072 GHz microwave radiometer measurements of the polar mesosphere and lower thermosphere from a high-latitude location at Ny-Ålesund over three years, from 2017 to 2020.  $\text{O}_3$  vertical profiles are determined using established retrieval techniques and measurement uncertainties estimated. Seasonally-averaged  $\text{O}_3$  profiles for night-time and twilight conditions are compared with the corresponding 9.6  $\mu\text{m}$  SABER observations to investigate uncertainties and biases in the mesospheric  $\text{O}_3$  satellite dataset. Daytime mesospheric  $\text{O}_3$  abundances are too low to be measured using the Ku-band microwave technique. Instead, overlapping daytime and twilight SABER 9.6  $\mu\text{m}$  and 1.27  $\mu\text{m}$  satellite observations are compared to confirm previously-reported differences between  $\text{O}_3$  derived from the two satellite infrared channels.



## 2 Methodology

The following sections describe the ground-based microwave radiometer configuration for observations of the Arctic polar atmosphere, the O<sub>3</sub> profile retrieval, and the method used for selecting overlapping SABER data.

### 95 2.1 Ground-based ozone measurements

#### 2.1.1 Instrument configuration

The Ny-Ålesund Ozone in the Mesosphere Instrument (NAOMI) is a development of the original MOSAIC 11.072 GHz O<sub>3</sub> radiometer configuration of Rogers et al. (2009). For NAOMI, input signals in the frequency band 10.7–11.7 GHz are collected by a 60 cm diameter satellite TV reflector dish (Primesat “Easy Fit” EF60) and down-converted to the 950–1950 MHz output  
100 range using a dual LNB feedhorn (LNBF, Star Com Communications Ku-band twin model SR-3602). An antenna beam efficiency of 0.74 is incorporated in the O<sub>3</sub> VMR retrieval. The beamwidth of the parabolic antenna, where microwave power is half (-3 dB) of the maximum value, is estimated to be 3.2° at the target frequency of 11.072 GHz. The LNBF outputs are filtered (Mini-Circuits VHF-740 high-pass filter, typical passband 780–2800 MHz), to minimise out-of-band interference, and attenuated. Two software defined radio (SDR) receivers (Type RTL2832U with R820T) capture a 2.5 MHz bandwidth from  
105 each linear polarisation of the LNBF. Measuring both horizontal and vertical polarisation outputs of the LNBF gives a  $\sqrt{2}$  improvement in signal-to-noise compared to measurements of a single polarisation. Frequency-switched spectra of the 11.072 GHz O<sub>3</sub> line are acquired every 60 s using an Intel® Next Unit of Computing (NUC) minicomputer. The spectral data are comprised of 256 channels, each of width 2.44 kHz, giving a total frequency bandwidth of 0.625 MHz. Frequency calibration is performed by measuring the frequency harmonic at 11.070 GHz generated by a 10 MHz oven crystal oscillator.

110

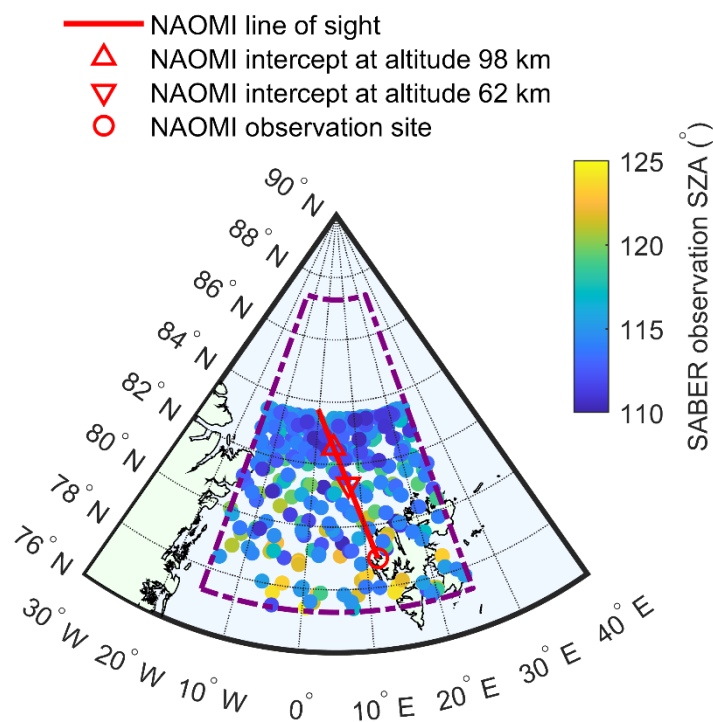
#### 2.1.2 NAOMI observations

Ground-based atmospheric observations using NAOMI are made from the UK Arctic Research Station (latitude 78°55'0" N, longitude 11°55'59" E) at Ny-Ålesund, Spitsbergen, which is part of the Svalbard archipelago. NAOMI observations have been made from this site since 4 July 2017. The antenna assembly is mounted on the external wall of a building at a height  
115 approximately 2 m above the ground. A clear, unobscured sky view is obtained with the antenna pointing at 11° elevation and azimuthal angle of 345°, with the line-of-sight NAOMI view shown in **Figure 1**. Transformation of local azimuth-elevation-range (AER) spherical coordinates for NAOMI to geodetic coordinates, specified by latitude, longitude, and altitude, used the World Geodetic System 1984 (WGS 84) reference ellipsoid. Pointing the instrument towards the north minimises pickup of interfering signals from geostationary satellites at low to mid-latitudes. Detected microwave signals from non-atmospheric  
120 sources such as satellites could lead to errors in the O<sub>3</sub> retrieval or, in a worst case, obscure the 11.072 GHz emission line.

NAOMI data were binned according to the local solar zenith angle (SZA) at 90 km into night-time (SZA > 110°), twilight (75° ≤ SZA ≤ 110°), and daytime (SZA < 75°) observations. Binned O<sub>3</sub> records between 15 August 2017 and 15 March 2020 were averaged for the following three periods: 15 December–15 March, 15 April–15 July, and 15 August–15 November. The



3-month periods, hereafter identified as ‘winter’, ‘summer’, and ‘autumn’ respectively, were chosen to overlap the SABER  
125 60-day yaw cycles rather than matching meteorological definitions of the seasons. NAOMI data were not recorded from 25  
September 2019 to 14 November 2019 due to a temporary instrument fault. Since averaging a smaller subset of valid  
observations between 15 August and 24 September 2019 would produce an O<sub>3</sub> spectrum with poorer signal-to-noise than using  
a complete three-month dataset, seasonal averages for autumn 2019 were not generated.



130

**Figure 1:** Map of Svalbard and the Arctic region poleward of geographic latitude 76° N and from 30° W to 40° E. The red circle shows the  
NAOMI ground-based location (78°55'0" N, 11°55'59" E). The red line is the projection of the line-of-sight view of NAOMI at elevation  
135 angle 11° and azimuth 345°. The dashed purple box shows the region ±20° longitude and ±5° latitude of the NAOMI intercept at altitude  
90 km (82°16'57" N, 5°6'50" E) used for selecting overlapping SABER observations. The filled, coloured circles show the locations and  
SZAs of SABER observations within the dashed purple box during night-time conditions (SZA at altitude 90 km > 110°) in the 2017–18  
winter (i.e., 15 December 2017–15 March 2018).

### 2.1.3 NAOMI ozone retrieval

140 Mesospheric O<sub>3</sub> profiles were retrieved from the NAOMI observations using version 2.2.58 of the Atmospheric Radiative  
Transfer Simulator (ARTS) (available at <http://www.radiativetransfer.org/>, last access: 8 August 2016) (Buehler et al., 2005,  
2018; Eriksson et al., 2011) and the Qpack2 (a part of atmlab v2.2.0) software package (Eriksson et al., 2005) using the optimal  
estimation method (OEM) (Rodgers, 2000). The configuration and spectroscopic inputs for the ARTS / Qpack2 optimal  
estimation retrieval was as described in Newnham et al. (2019). Vertical profiles of O<sub>3</sub> VMR were calculated using a 10-year



145 dataset from WACCM-D (Verronen et al., 2016) covering 2000–2009. WACCM-D is a 3-D global atmospheric model that  
incorporates a detailed representation of D-region chemistry in the specified dynamics (SD) version of the Whole Atmosphere  
Community Climate Model (WACCM 4) (Marsh et al., 2013). The WACCM-D data at 78.632 °N and 12.500 °E, the model  
grid point closest to Ny-Ålesund, were used. Water vapour (H<sub>2</sub>O) VMR profiles were a combination of 6 hourly, model level  
Modern-Era Retrospective analysis for Research and Applications, Version 2 (MERRA-2) data (download date: 18 April 2020)  
150 and WACCM-D data. MERRA-2 H<sub>2</sub>O data were selected at pressure levels below 10<sup>-2</sup> hPa overlapping NAOMI observations,  
for the reanalysis grid point at latitude 79.000 °N and longitude 11.875 °E closest to the instrument location and combined  
with WACCM-D data for higher altitudes (i.e., at pressures below 10<sup>-2</sup> hPa). Similarly, temperature profiles were constructed  
by combining MERRA-2 data at atmospheric levels below 10<sup>-2</sup> hPa, SABER version 2.0 data (downloaded from  
ftp://saber.gats-inc.com/custom/Temp\_O3\_H2O/v2.0/; Last access: 30 April 2020) between 10<sup>-2</sup> hPa and 10<sup>-4</sup> hPa, and  
155 WACCM-D data at pressures below 10<sup>-4</sup> hPa. The inclusion of SABER data provides more realistic mesospheric temperatures  
than WACCM-D averages, in particular following the sudden stratospheric warmings of 12 February 2018 and 2 January 2019  
when mesospheric temperatures decreased by up to 40 K.

## 2.2 SABER ozone data

SABER version 2.0 temperature, O<sub>3</sub> VMR, and water vapour VMR profiles (downloaded from ftp://saber.gats-  
160 inc.com/custom/Temp\_O3\_H2O/v2.0/; Last update: 30 April 2020) were used in the analysis. SABER profiles were selected  
where the tangent point at 90 km is within ±20° longitude and ±5° latitude of the calculated NAOMI measurement co-ordinates  
(82°16'57" N, 5°6'50" E). The 90 km altitude is chosen as it is the approximate mesopause height and below the secondary  
O<sub>3</sub> VMR maximum. The locations of night-time SABER profiles for the 2017–18 winter are shown in **Figure 1**. The SABER  
observations overlap the NAOMI line-of-sight path and are more tightly clustered towards the northerly extent of 83.5° N.  
165 The SABER observations in the defined region were then binned into night-time, twilight, and daytime datasets for the defined  
winter, summer, and autumn periods, as was done for the NAOMI data. The SZAs at 90 km for the binned regions, plotted in  
**Figure 2**, show that daytime SABER observations are restricted to the summer periods and the start of autumn whereas  
night-time measurements occur at the end of autumn and during winter.

## 3 Results

170 The NAOMI O<sub>3</sub> vertical profile retrieval and estimated uncertainties are presented and discussed in **Sect. 3.1**, using the 2017–  
18 winter night-time case as an example. The NAOMI and SABER 9.6 μm O<sub>3</sub> vertical profiles for winter night-time, winter  
twilight, and autumn twilight periods are compared in **Sect. 3.2**. SABER 9.6 μm and 1.27 μm observations overlap in the  
region of the NAOMI measurements during summer daytime and twilight conditions in summer and autumn, and the selected  
portions of the satellite datasets during 2017, 2018, and 2019 are compared in **Sect. 3.3**.

175

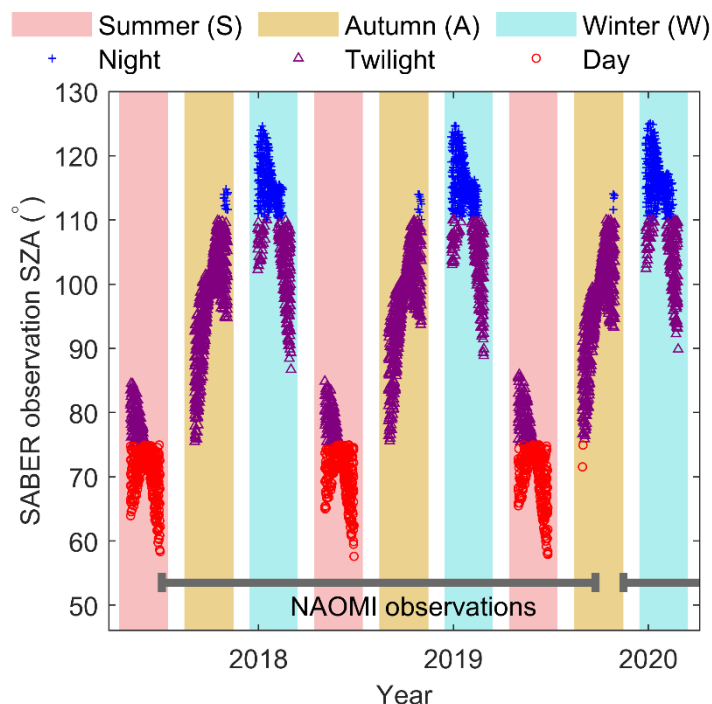


**Figure 2:** SZA of SABER observations at 90 km altitude with spatial overlap of the NAOMI measurements. The plotted SABER observations, covering the period from 27 March 2017 to 5 April 2020, are a subset of the full SABER dataset. SABER observations during night-time (SZA at altitude 90 km > 110°), twilight (75° ≤ SZA at altitude 90 km ≤ 110°), and daytime conditions (SZA at altitude 90 km < 75°) are shown by blue '+' symbols, purple triangles, and red circles, respectively. Red, orange, and blue shaded regions indicate nominal summer (15 April–15 July), autumn (15 August–15 November), and winter (15 December–15 March) periods, respectively. The grey horizontal bars show the periods when NAOMI observations were made.

### 3.1 Ozone retrieval

Ozone retrievals were performed for the winter and autumn night-time, and autumn twilight, periods where mesospheric O<sub>3</sub> abundances were higher than during sunlit conditions. The retrieval results for the 2017–18 winter night-time are shown in **Figure 3**. **Figure 3a** compares the final retrieval fit (red line) with the measured O<sub>3</sub> spectrum (black line), with the residual differences shown in **Figure 3b** in agreement to within the rms baseline noise level. **Figure 3c** shows the retrieved (red line) and a priori (black line) O<sub>3</sub> VMR profiles. The retrieval altitude range, where information is obtained from the observations, is indicated by the thicker solid lines and shaded grey areas and is determined as described in the next paragraph. Outside of the retrieved altitude range the O<sub>3</sub> VMRs approach the a priori values.

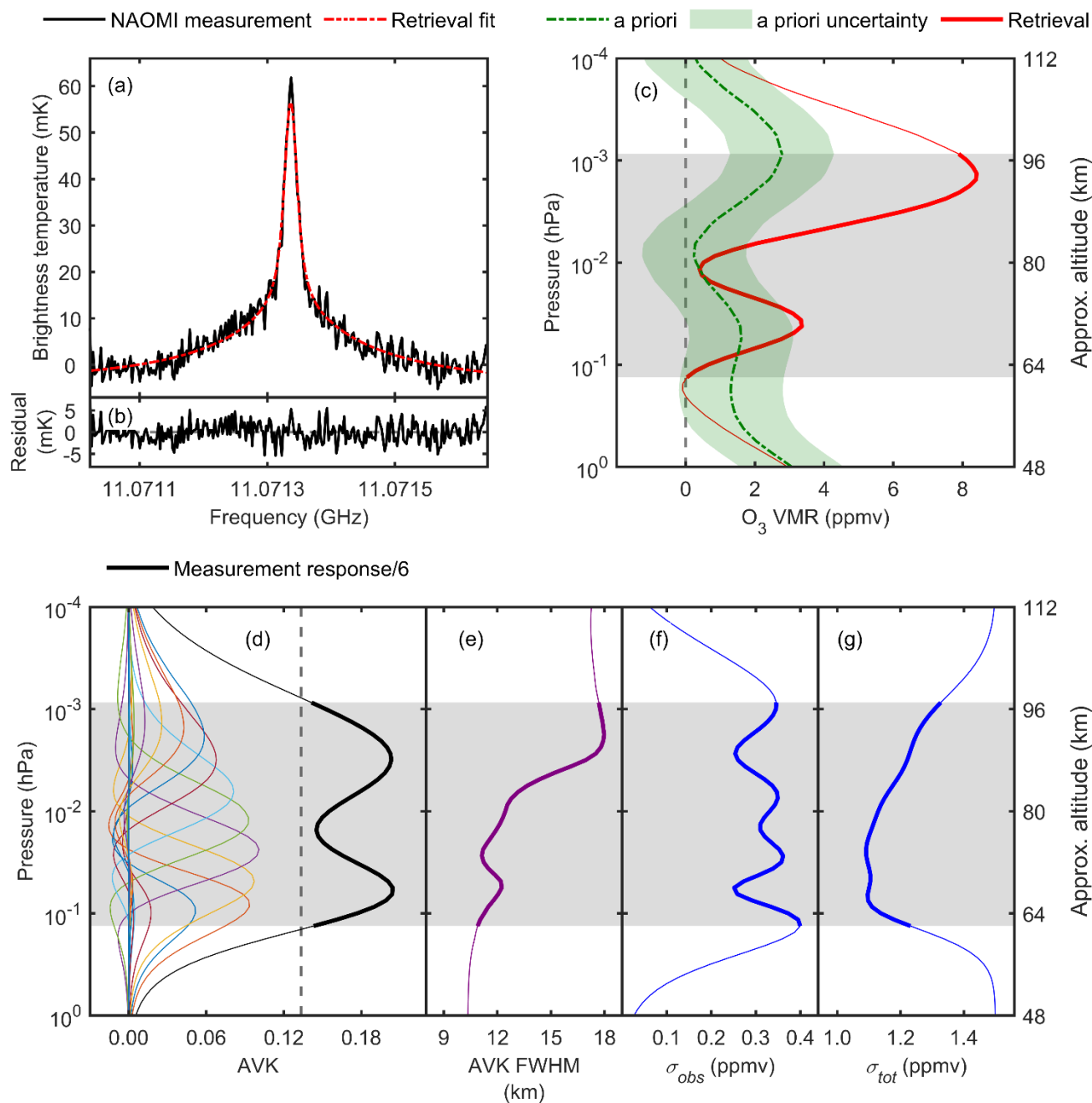


**Figure 3:** Ozone (O<sub>3</sub>) retrieval for NAOMI observations during 2017–18 winter night-time (15 December 2017–15 March 2018, SZA at altitude 90 km > 110°). The seasonal mean O<sub>3</sub> spectrum and retrieval fit is shown in (a), and the residual differences are shown in (b). The a priori and retrieved O<sub>3</sub> volume mixing ratio profiles are shown in (c), where the green shading represents the a priori uncertainty (±1.5 ppmv). In (d) every sixth averaging kernel and the scaled measurement response (MR) are shown, with the vertical grey dashed line showing the cut-off for MR ≥ 0.8. Panel (e) shows the full-width half maxima of each averaging kernel (AVK FWHM). The measurement uncertainty (σ<sub>obs</sub>) and total uncertainty (σ<sub>tot</sub>) are shown in (f) and (g) respectively. The grey shaded regions and thicker sections of the plotted curves in (c)–(g) indicate the pressure and altitude ranges where MR ≥ 0.8.



The averaging kernels (AVKs) for every sixth retrieved altitude are shown in **Figure 3c**. The AVKs describe the relationship between the true, a priori, and retrieved atmospheric states (Rodgers, 2000) and can be used to indicate the altitudes over which  $O_3$  is observed and the height resolution. The sum of the AVKs at each altitude is the measurement (or total) response (MR), which represents the contribution of the measurement to the retrieval solution compared to the a priori influence at that altitude (Christensen and Eriksson, 2013). The altitude range where the retrieved  $O_3$  profile has a high degree of independence from the a priori is identified by MR values higher than 0.8. The retrieval pressure (altitude) range where the  $MR \geq 0.8$  criterion is met is  $9 \times 10^{-4}$ –0.13 hPa ( $\sim 97$ –62 km), shown by the thicker sections of the lines and the shaded grey areas in **Figures 3b–g**. Outside of these altitudes (i.e., below 62 km and above 97 km) MR is  $< 0.8$  and  $O_3$  values should be interpreted with caution as the information from the a priori becomes important. In the ideal case the AVKs would be delta functions but in practice they are peaked functions with finite widths dependent on the spatial resolution of the observing system. The full-width half-maximum (FWHM) widths of the kernels provide a measure of the vertical resolution of the retrieved profile. The FWHM values shown in **Figure 3e** indicate the altitude resolution is worst at 18.0 km at  $\sim 90$  km and improves with decreasing altitude to 10.9 km at 62 km in the lower mesosphere. The altitude resolution can also be estimated from the degrees of freedom for signal (DOFS) for the inversion, given by the trace of the AVK matrix (Rodgers, 2000; Ryan and Walker, 2015). Dividing the retrieved altitude range ( $\sim 35$  km) by the DOFS ( $\sim 2.9$ ) over the same range gives an altitude resolution of 12.1 km, within the range of AVK FWHM values.

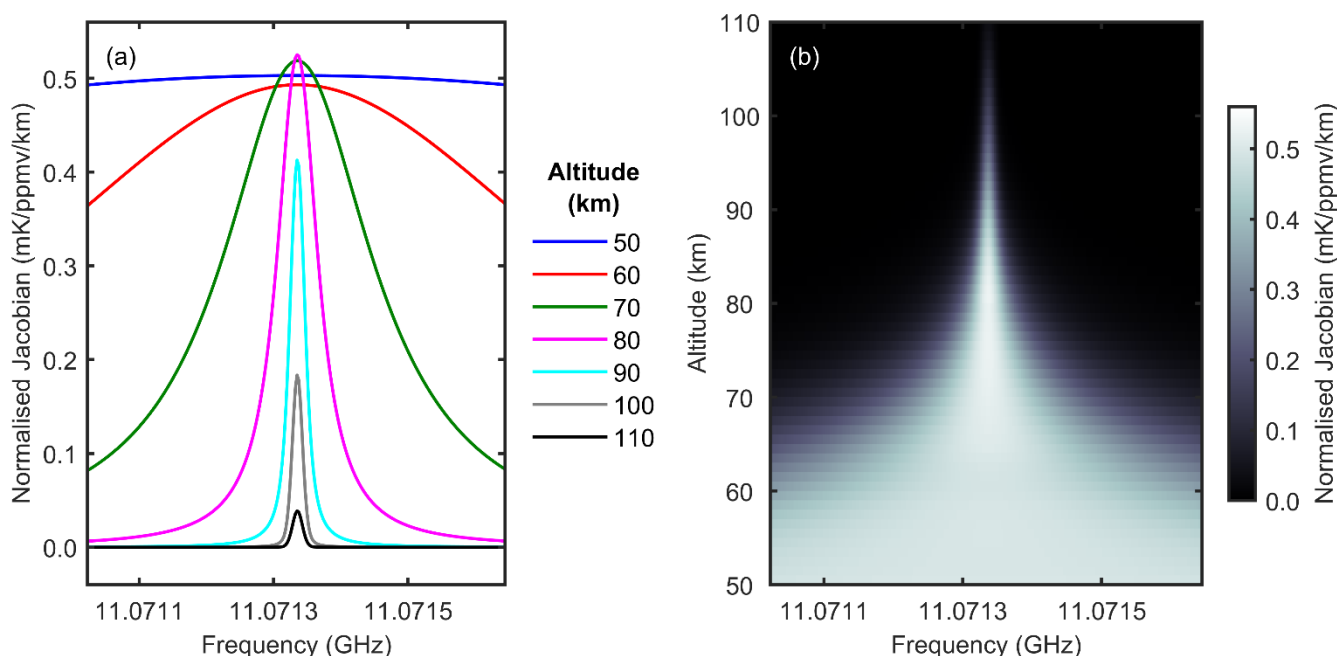


**Figure 4:** Jacobian matrix describing the NAOMI ozone ( $O_3$ ) retrieval, normalised by the layer thickness of the retrieval grid. The data are for observations during 2017–18 winter night-time (15 December 2017–15 March 2018, SZA at altitude 90 km  $> 110^\circ$ ). Rows of the Jacobian matrix for selected altitude levels are plotted in (a). The grey scale in (b) indicates the values of the Jacobian matrix.



Observation errors ( $\sigma_{obs}$ ) and total retrieval (observation plus smoothing) errors ( $\sigma_{tot}$ ) from the OEM retrievals provide further estimates of the retrieved profile uncertainty. The observation errors describe how the retrieved profiles are affected by measurement noise and are shown in **Figure 3f**, with mean value 0.32 ppmv. Observation errors decrease above and below the AVK peaks as the retrieval tends towards the a priori and the measurement contribution is small in these regions. The total retrieval errors shown in **Figure 3g** are in the range 1.09–1.33 ppmv, with mean value 1.17 ppmv, and tend towards the a priori uncertainty of 1.5 ppmv outside the range of AVK peaks.

The values of the Jacobian matrix of the O<sub>3</sub> forward model, normalised by the layer thickness of the retrieval grid, are shown in **Figure 4**. Normalised Jacobian values close to the centre of the 11.072 GHz emission line are in the range 0.4–0.5 mK (ppmv)<sup>-1</sup>km<sup>-1</sup> at mesospheric altitudes 60–90 km. At higher altitudes, above 90 km, the gain response is weaker and spread over a narrow range of frequencies due to negligible pressure broadening of the emission line.

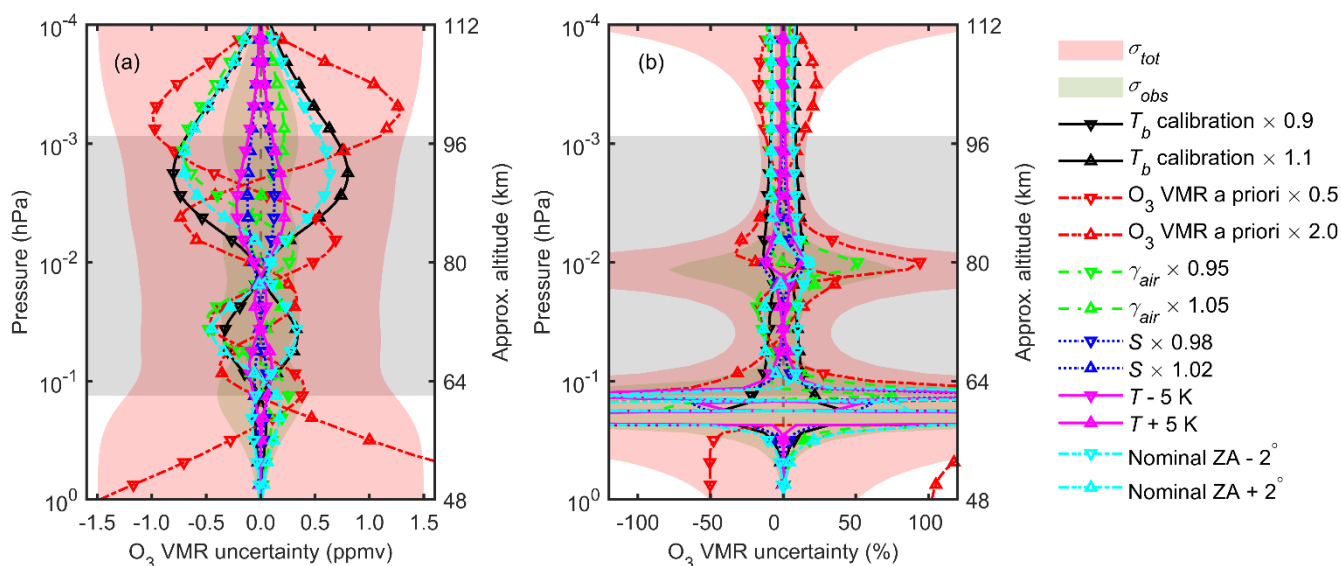


**Figure 5:** Estimated uncertainties in the ozone (O<sub>3</sub>) retrieval for NAOMI observations during winter 2017–18 night-time (15 December 2017–15 March 2018, SZA at altitude 90 km > 110°). Absolute O<sub>3</sub> VMR uncertainties are shown in (a) and relative (%) uncertainties in (b). The grey shaded regions indicate the pressure and altitude ranges where MR  $\geq 0.8$ .

Contributions to uncertainties in the O<sub>3</sub> retrieval were determined by comparing the night-time, 2017–18 winter profiles from separate runs where input parameters were perturbed from their nominal values in turn. The adjusted parameters were brightness temperature calibration ( $T_b \pm 10\%$  for all observed frequencies), air broadening coefficient of the O<sub>3</sub> line ( $\gamma_{air} \pm 5\%$ ), O<sub>3</sub> line intensity ( $S \pm 2\%$ ), and observation zenith angle (nominal ZA  $\pm 2^\circ$ ). A priori O<sub>3</sub> VMR values were scaled by 0.5 and 2.0 at all pressure levels, and the temperature profile perturbed by  $\pm 5$  K. The differences between the retrieved O<sub>3</sub> profiles



from the perturbed and nominal runs are shown in **Figures 5a and 5b** as absolute VMR (ppmv) and percentage uncertainties, respectively. The uncertainty contributions are within the envelope of total retrieval uncertainty, shown by the red shading, over the range of retrieved altitudes. The largest absolute error of  $\pm 0.80$  ppmv at  $\sim 90$ – $95$  km is from the estimated 10% radiometric calibration error, followed by zenith angle and  $O_3$  a priori uncertainties above 80 km. The largest percentage uncertainties, exceeding 94%, are at  $\sim 62$  km and 80 km where the VMR is close to zero.

### 250 3.2 Comparison of NAOMI and SABER mesospheric ozone profiles

The  $O_3$  vertical profiles for winter night-time, winter twilight, and autumn twilight periods where the NAOMI and SABER 9.6  $\mu\text{m}$  datasets overlap are shown in **Figures 6, 7, and 8**, respectively. The seasonal mean SABER profiles were smoothed using the NAOMI AVK's for direct comparison with the ground-based observations, and absolute VMR and percentage differences calculated.  $O_3$  number densities were calculated from the NAOMI and SABER 9.6  $\mu\text{m}$   $O_3$  VMR profiles using pressures and temperatures from the combined MERRA-2, SABER, and WACCM-D profiles constructed for the NAOMI retrievals. The number densities were integrated to determine the  $O_3$  partial columns over altitudes 62–80 km, 80–98 km, and the full NAOMI retrieval range of 62–98 km as shown in **Figure 9**.

The night-time  $O_3$  VMR profiles for the 2017–18, 2018–19, and 2019–20 winters are compared in **Figure 6** and **Table 1**. For both NAOMI and SABER data, the secondary  $O_3$  peak VMR values are higher in the 2017–18 and 2019–20 winters than in 2018–19. For NAOMI, the highest secondary maximum is 10.7(13) ppmv for the 2019–20 winter compared to 8.3(13) ppmv for the previous, 2018–19 winter. The tertiary maxima are similar for each of the three winters but the tertiary  $O_3$  layers from NAOMI are narrower than those measured by SABER, and more sharply peaked with maximum VMR 31%–52% higher. The tertiary and secondary maxima in the NAOMI VMR profiles are at 69–70 km and 93–94 km respectively, 1–2 km lower in altitude than SABER. The largest percentage differences occur at  $\sim 64$  km and 80 km due to very low ( $< 0.2$  ppmv)  $O_3$  VMR at these altitudes.

The average  $O_3$  profiles for the three twilight winters, presented in **Figure 7** and **Table 2**, show a similar pattern to the night-time winters with secondary  $O_3$  peak VMR values higher in the 2017–18 and 2019–20 winters than in 2018–19. However, the secondary maximum VMRs for winter twilight are 6–26% smaller, apart from the SABER 2018–19 twilight peak which is 8% larger than the corresponding night-time value. The most significant differences between NAOMI and SABER observations are found in the autumn twilight  $O_3$  profiles (**Figure 8** and **Table 3**) at secondary layer altitudes in the range 88–97 km. The NAOMI secondary maximum VMR is 47% and 59% of the SABER peak value for the two years where these measurements were made, 2017 and 2018 respectively. The largest differences are at altitudes above 88 km, in the secondary  $O_3$  layer, whereas below 88 km the NAOMI and SABER profiles agree to within the measurement uncertainties.

275

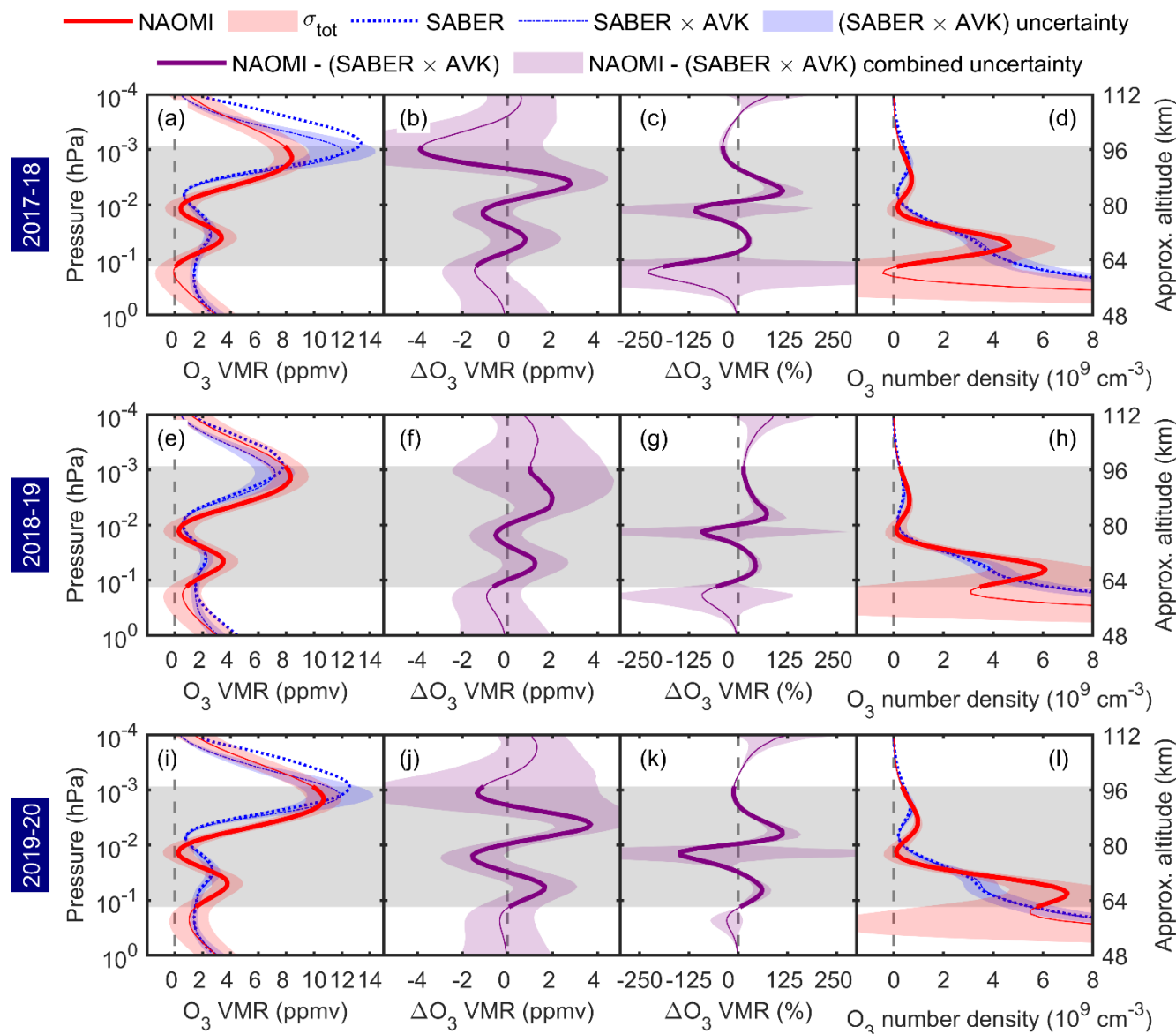


Year(s)	Secondary O <sub>3</sub> peak				Tertiary O <sub>3</sub> peak			
	NAOMI		SABER		NAOMI		SABER	
	O <sub>3</sub> VMR (ppmv)	Altitude (km)	O <sub>3</sub> VMR (ppmv)	Altitude (km)	O <sub>3</sub> VMR (ppmv)	Altitude (km)	O <sub>3</sub> VMR (ppmv)	Altitude (km)
2017–18	8.4(13)	94	12.0(24)	95	3.4(11)	70	2.6(5)	71
2018–19	8.3(13)	94	7.2(14)	95	3.5(11)	69	2.3(5)	70
2019–20	10.7(13)	93	11.9(24)	94	3.8(11)	69	2.7(5)	72

**Table 1:** Secondary and tertiary ozone peak VMR and altitudes from NAOMI and SABER 9.6 μm observations during winter night-time (15 December–15 March, SZA at altitude 90 km > 110°) for 2017–18, 2018–19, and 2019–20. The figures in parentheses after the VMR values are uncertainties.

Year(s)	Secondary O <sub>3</sub> peak				Tertiary O <sub>3</sub> peak			
	NAOMI		SABER		NAOMI		SABER	
	O <sub>3</sub> VMR (ppmv)	Altitude (km)	O <sub>3</sub> VMR (ppmv)	Altitude (km)	O <sub>3</sub> VMR (ppmv)	Altitude (km)	O <sub>3</sub> VMR (ppmv)	Altitude (km)
2017–18	7.9(13)	94	8.8(18)	94	4.0(11)	70	2.7(5)	73
2018–19	6.9(13)	94	7.8(16)	95	3.0(11)	71	2.1(4)	69
2019–20	9.5(13)	94	10.7(21)	95	3.8(11)	70	2.9(5)	73

**Table 2:** Secondary and tertiary ozone peak VMR and altitudes from NAOMI and SABER 9.6 μm observations during winter twilight (15 December–15 March, 75° ≤ SZA at altitude 90 km ≤ 110°) for 2017–18, 2018–19, and 2019–20. The figures in parentheses after the VMR values are uncertainties.



290 **Figure 6:** Mean ozone vertical profiles from NAOMI and SABER 9.6  $\mu\text{m}$  observations during winter night-time (15 December–15 March, SZA at altitude 90 km > 110°) in 2017–18 (a–d), 2018–19 (e–h), and 2019–20 (i–l). The second and third columns give the absolute and relative (%) differences (NAOMI minus SABER 9.6  $\mu\text{m}$ ). The red, blue, and purple shading are the estimated uncertainties of the plotted parameters. The grey shaded regions and thicker sections of the plotted curves indicate the pressure and altitude ranges where MR  $\geq$  0.8.

295

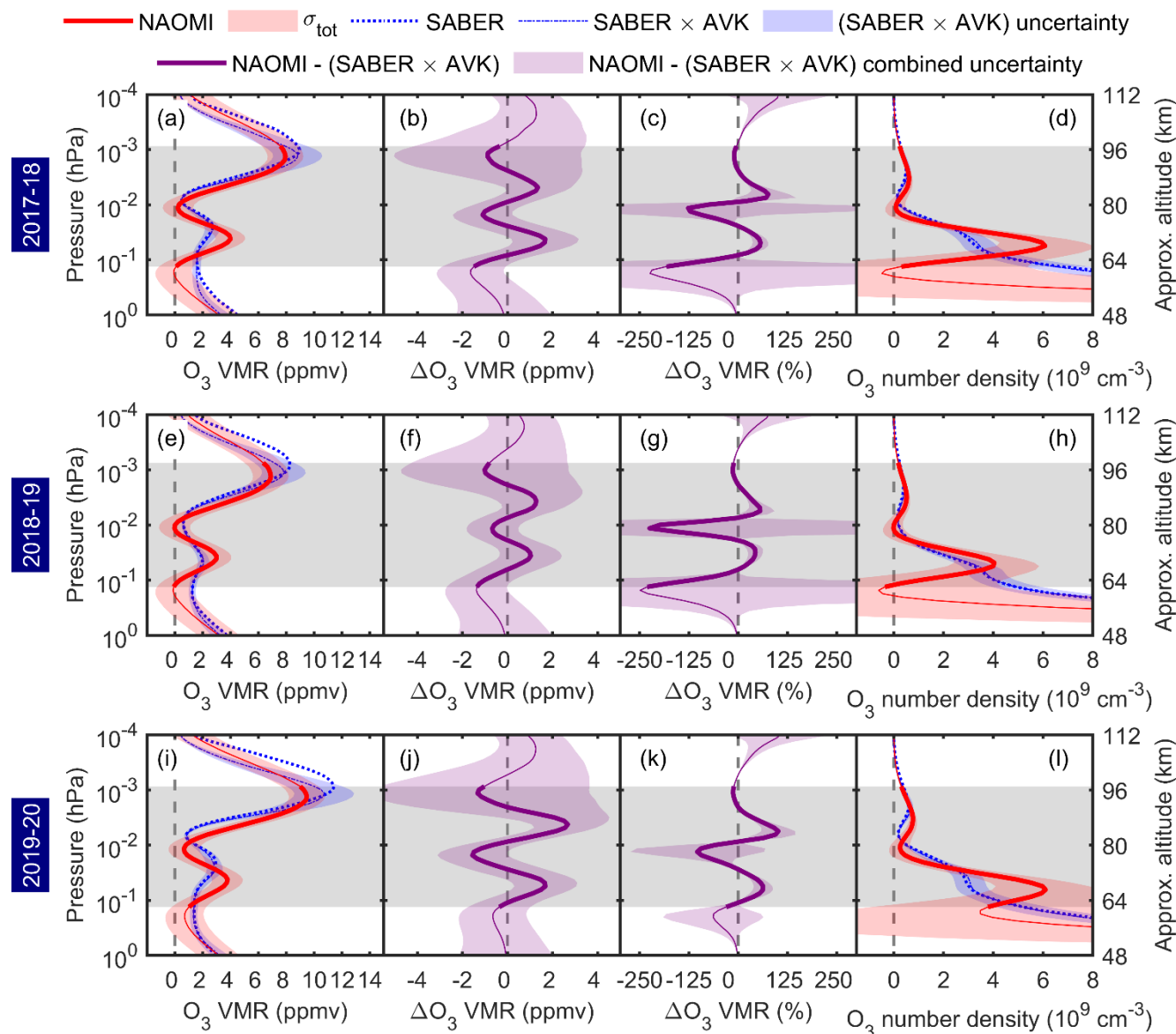


**Figure 7:** Mean ozone vertical profiles from NAOMI and SABER 9.6  $\mu\text{m}$  observations during winter twilight (15 December–15 March,  $75^\circ \leq \text{SZA}$  at altitude  $90 \text{ km} \leq 110^\circ$ ) in 2017–18 (a–d), 2018–19 (e–h), and 2019–20 (i–l). The second and third columns give the absolute and relative (%) differences (NAOMI minus SABER 9.6  $\mu\text{m}$ ). The red, blue, and purple shading are the estimated uncertainties of the plotted parameters. The grey shaded regions and thicker sections of the plotted curves indicate the pressure and altitude ranges where  $\text{MR} \geq 0.8$ .

300

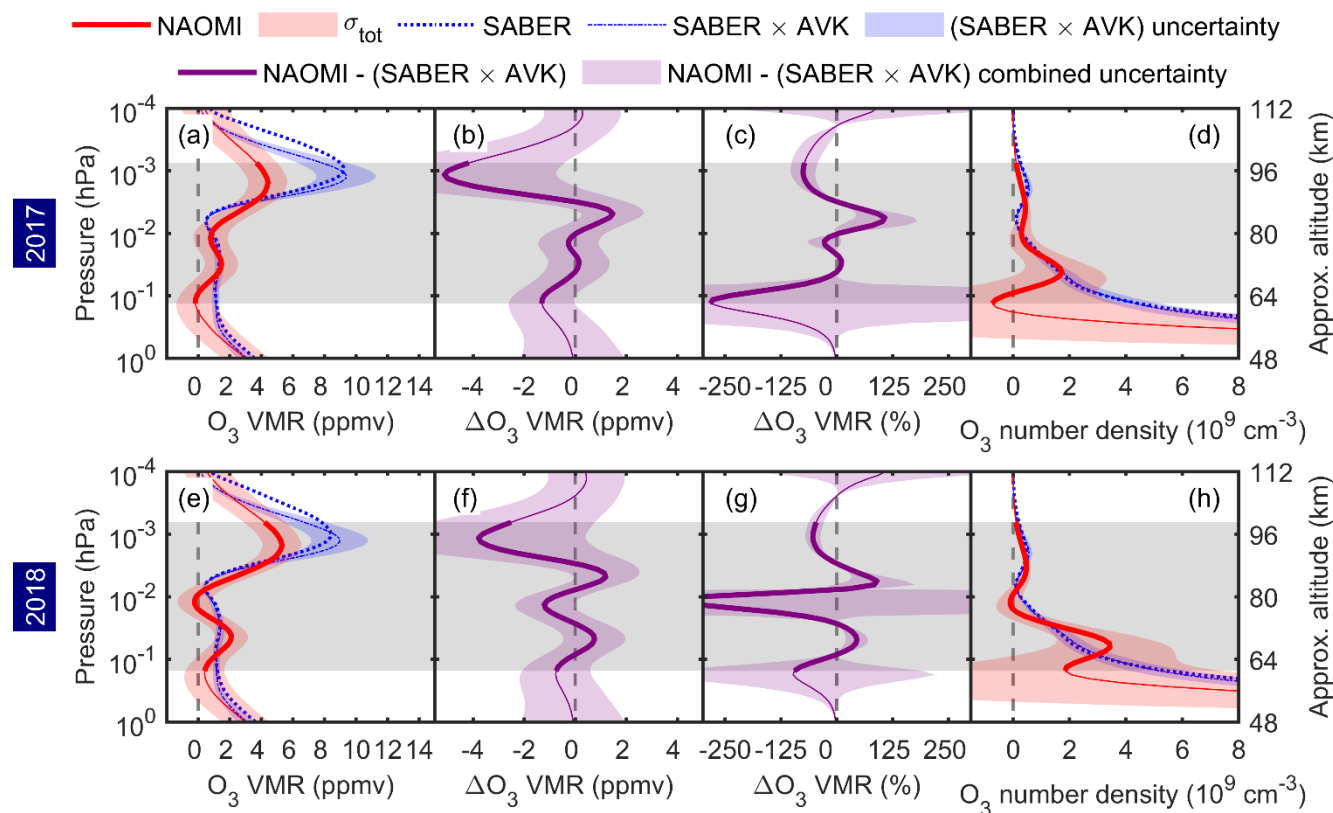
305



Year(s)	Secondary O <sub>3</sub> peak				Tertiary O <sub>3</sub> peak			
	NAOMI		SABER		NAOMI		SABER	
	O <sub>3</sub> VMR (ppmv)	Altitude (km)	O <sub>3</sub> VMR (ppmv)	Altitude (km)	O <sub>3</sub> VMR (ppmv)	Altitude (km)	O <sub>3</sub> VMR (ppmv)	Altitude (km)
2017	4.4(12)	93	9.4(19)	95	1.5(10)	72	1.3(3)	71
2018	5.3(12)	93	9.0(18)	94	2.1(10)	70	1.4(3)	72

**Table 3:** Secondary and tertiary ozone peak VMR and altitudes from NAOMI and SABER 9.6  $\mu\text{m}$  observations during autumn twilight (15 September–15 November,  $75^\circ \leq \text{SZA}$  at altitude  $90 \text{ km} \leq 110^\circ$ ) in 2017 and 2018. The figures in parentheses after the VMR values are uncertainties.

310

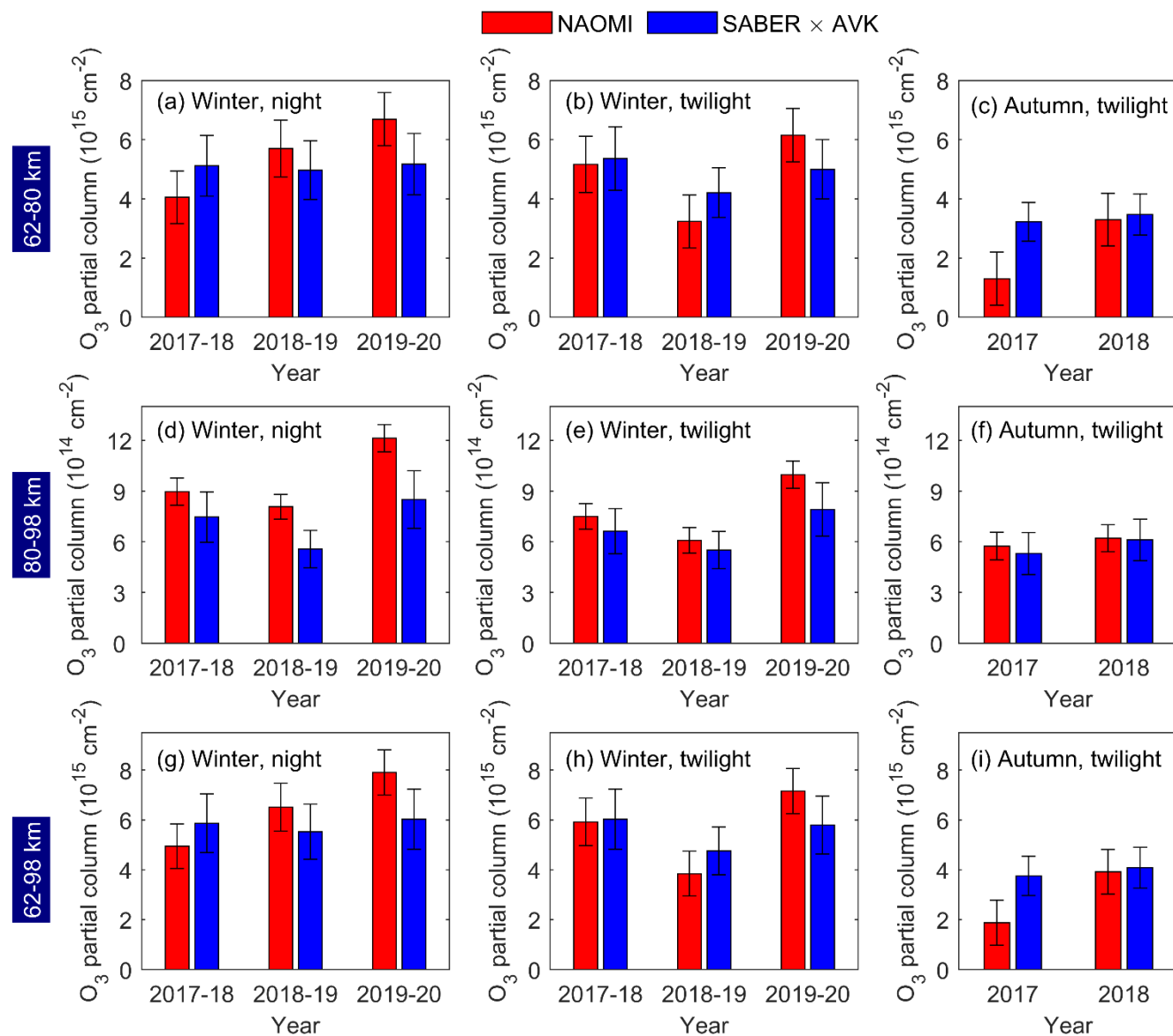


315

**Figure 8:** Mean ozone vertical profiles from NAOMI and SABER 9.6  $\mu\text{m}$  observations during autumn twilight (15 September–15 November,  $75^\circ \leq \text{SZA}$  at altitude  $90 \text{ km} \leq 110^\circ$ ) in 2017 (a–d) and 2018 (e–h). The second and third columns give the absolute and relative (%) differences (NAOMI minus SABER 9.6  $\mu\text{m}$ ). The red, blue, and purple shading are the estimated uncertainties of the plotted parameters. The grey shaded regions and thicker sections of the plotted curves indicate the pressure and altitude ranges where  $\text{MR} \geq 0.8$ .



The NAOMI and SABER O<sub>3</sub> partial columns are shown in **Figure 9** for winter night and autumn night and twilight conditions in the different years. The columns over 62–80 km (**Figures 9a–c**) are up to an order of magnitude higher than over 80–98 km (**Figures 9d–f**) and are generally higher in the winter night and twilight cases (**Figures 9a–b, 9d–e, 9g–h**) than in autumn twilight (**Figures 9c, f, i**) where lower SZA conditions and correspondingly higher solar irradiance decrease middle atmospheric O<sub>3</sub> abundance. Observations by the two instruments show a similar pattern of variability from year to year, with the highest O<sub>3</sub> columns in the 2019–20 winter. The columns measured by the two instruments agree to within the measurement uncertainties shown by the vertical error bars, apart from the 2018–19 and 2019–20 winter nights at 80–98 km and for the 2017 autumn twilight at 62–80 km. Over the full retrieved altitude range (62–98 km), the NAOMI column for the 2017 autumn twilight is 51% smaller than the corresponding SABER measurement. The largest contribution to the difference is at 62–80 km (**Figure 9c**), whereas the smaller columns over 80–98 km (**Figure 9f**) are in good agreement as are the 2018 data (**Figure 9c, 9f, and 9i**). The large discrepancy between the autumn 2017 NAOMI and SABER observations could be due to a significant spectrum baseline ripple during the initial months of NAOMI operation. This possible cause is also indicated by the larger deviation of NAOMI O<sub>3</sub> number density, which is integrated to produce partial columns, from the smoothed SABER profile for 2017 (**Figure 8d**) compared to 2018 (**Figure 8h**). As indicated by the retrieval Jacobians (**Figure 4**), smoothly-varying offsets and distortions over the 0.625 MHz NAOMI spectral bandwidth will affect O<sub>3</sub> retrieval for the lower mesosphere whereas the narrow band gaussian signal corresponding to O<sub>3</sub> emission above ~80 km will be less affected.



335 **Figure 9:** Mean ozone partial columns at 62–80 km (a–c), 80–98 km (d–f), and 62–98 km (g–i) from NAOMI and SABER 9.6  $\mu\text{m}$  observations during night-time winter (left column), winter twilight (centre column), and autumn twilight (right column) conditions in 2017–20. The error bars are the estimated uncertainties of the plotted parameters. Note that the partial column scales for the upper (a–c), middle (d–f), and lower (g–i) panel plots differ.



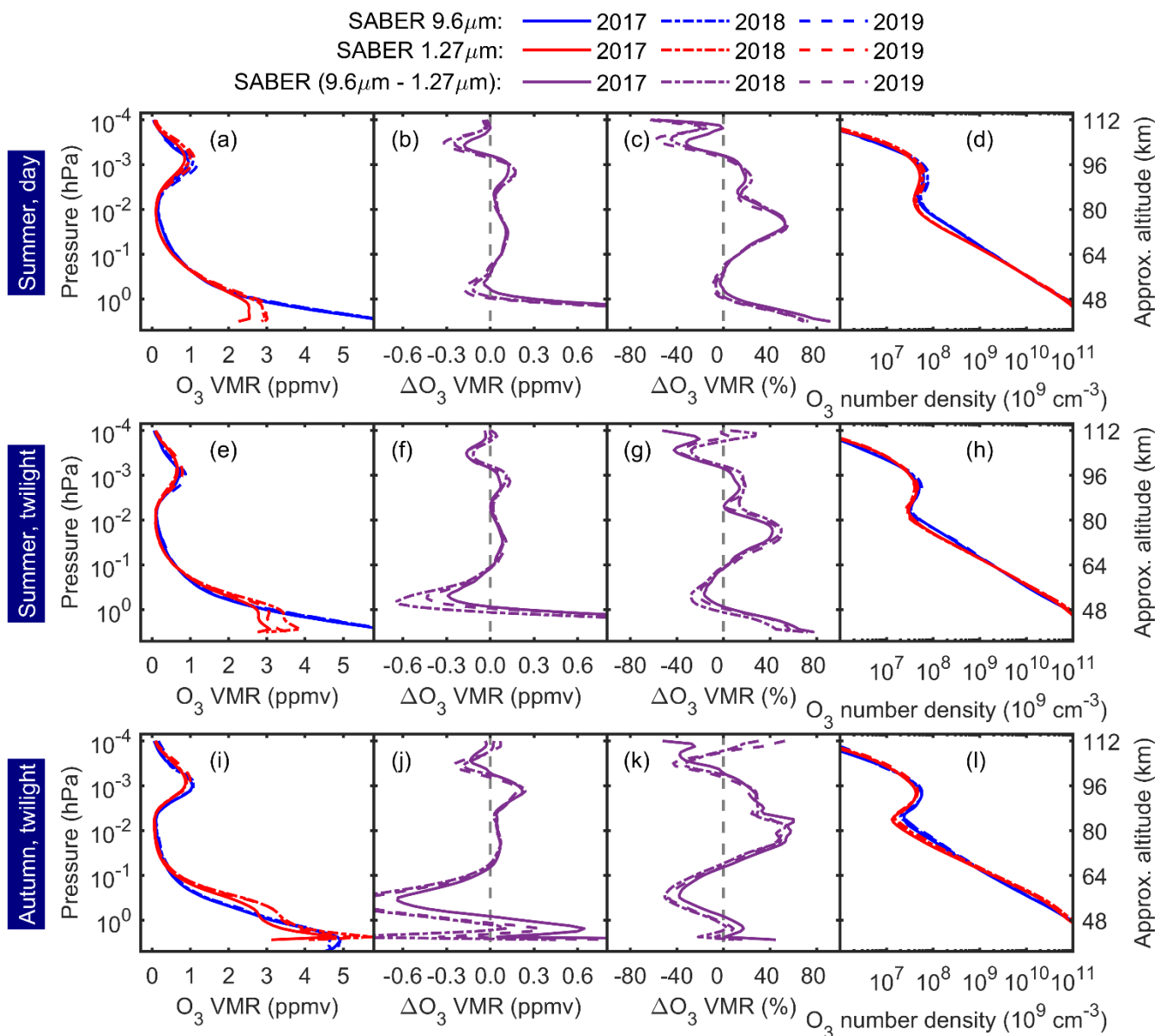
### 3.3 SABER 9.6 $\mu\text{m}$ and 1.27 $\mu\text{m}$ ozone profiles

340 The overlapping  $\text{O}_3$  profile data from SABER 9.6  $\mu\text{m}$  and 1.27  $\mu\text{m}$  observations during daytime in summer and twilight in  
 summer and autumn are compared in **Figure 10** and **Table 4**. The secondary  $\text{O}_3$  maximum from both SABER channels show  
 a similar pattern, with larger peak VMR for all three cases in 2019 compared to the two previous years. However, SABER  
 9.6  $\mu\text{m}$   $\text{O}_3$  VMR consistently exceeds SABER 1.27  $\mu\text{m}$  over 65–95 km with the largest difference (up to 58%) during autumn  
 345 and autumn twilight and by as much as 50% lower at  $\sim 56$  km in autumn twilight. The altitude of the secondary  $\text{O}_3$  maximum  
 in  $\text{O}_3$  mixing ratio is 90–92 km during day and 95 km at night. The secondary maximum in VMR in the SABER 9.6  $\mu\text{m}$   
 measurements is at 96–97 km,  $\sim 1$ –2 km lower than the corresponding SABER 1.27  $\mu\text{m}$  data.

		SABER 9.6 $\mu\text{m}$		SABER 1.27 $\mu\text{m}$	
	Year(s)	$\text{O}_3$ VMR (ppmv)	Altitude (km)	$\text{O}_3$ VMR (ppmv)	Altitude (km)
Summer, day	2017	0.95	97	0.85	98
	2018	1.07	97	0.99	99
	2019	1.18	96	1.10	98
Summer, twilight	2017	0.71	97	0.67	98
	2018	0.73	97	0.64	98
	2019	0.88	96	0.79	97
Autumn, twilight	2017	1.05	96	0.87	97
	2018	1.08	96	0.90	97
	2019	1.11	96	1.00	98

350

**Table 4:** Secondary ozone peak VMR and altitudes from SABER 9.6  $\mu\text{m}$  and 1.27  $\mu\text{m}$  observations during summer daytime (15 April–15 July,  $\text{SZA}$  at altitude  $90 \text{ km} < 75^\circ$ ), summer twilight (15 April–15 July,  $75^\circ \leq \text{SZA}$  at altitude  $90 \text{ km} \leq 110^\circ$ ), and autumn twilight (15 September–15 November,  $75^\circ \leq \text{SZA}$  at altitude  $90 \text{ km} \leq 110^\circ$ ).



355

**Figure 10:** Mean ozone vertical profiles from SABER 9.6  $\mu\text{m}$  and 1.27  $\mu\text{m}$  observations during (a–d) summer daytime (15 April–15 July, SZA at altitude 90 km < 75°), (e–h) summer twilight (15 April–15 July, 75° ≤ SZA at altitude 90 km ≤ 110°), and (i–l) autumn twilight (15 September–15 November, 75° ≤ SZA at altitude 90 km ≤ 110°). The second and third columns give the absolute and relative (%) differences (SABER 9.6  $\mu\text{m}$  minus SABER 1.27  $\mu\text{m}$ ).

360



#### 4 Conclusions

Seasonal O<sub>3</sub> vertical profiles in the Arctic polar MLT region (altitude range 62–98 km) have been retrieved from ground-based Ku-band microwave (NAOMI) atmospheric observations from Ny-Ålesund during 2017–20. The NAOMI observations show broadly the same year-to-year and seasonal O<sub>3</sub> variabilities as overlapping satellite data (version 2.0) from the SABER 9.6 μm channel during night-time and twilight conditions. The winter night-time and twilight NAOMI and SABER 9.6 μm O<sub>3</sub> VMR profiles agree but differences in the secondary O<sub>3</sub> region at 88–97 km during autumn twilight exceed the measurement uncertainties. The SABER secondary maximum VMR values are higher by 47% and 59% respectively compared to NAOMI for the two years, 2017 and 2018, where autumn twilight measurements were made. Considering the two SABER infrared channels which measure O<sub>3</sub> at different wavelengths and use different processing schemes, the autumn twilight SABER 9.6 μm O<sub>3</sub> VMRs for the three years 2017–19 are higher than the corresponding overlapping 1.27 μm measurements, with the largest difference of 58% over the altitude range 65–95 km similar to that between SABER 9.6 μm O<sub>3</sub> and the NAOMI observation. The SABER 9.6 μm O<sub>3</sub> summer daytime mesospheric O<sub>3</sub> VMR is also consistently higher than the 1.27 μm measurement. Our intercomparison between ground-based microwave observations and the two SABER O<sub>3</sub> channels builds on a previous study (Smith et al., 2013) where SABER 9.6 μm mesospheric O<sub>3</sub> showed good relative agreement with other satellite measurements (<10% difference) but daytime O<sub>3</sub> over the altitude range 60–80 km was biased 20–50% higher. Our new analysis of ground-based (NAOMI) observations and SABER datasets confirm the previously reported level of agreement between night-time SABER 9.6 μm mesospheric O<sub>3</sub> and other satellite datasets but show that under twilight conditions the 9.6 μm observations of secondary O<sub>3</sub> peak VMR are ~50% higher than both the SABER 1.27 μm and NAOMI measurements.

380

*Data availability.* The processed NAOMI and SABER datasets (Newnham et al., 2021) used in this study are available from the UK Polar Data Centre (<https://www.bas.ac.uk/data/uk-pdc/>). SABER data used in this study can be downloaded from [ftp://saber.gats-inc.com/Version2\\_0/Level2A/](ftp://saber.gats-inc.com/Version2_0/Level2A/). The presented data can be downloaded from xx (last access: xx xxx xxxx) [Authors' note: Datasets are available for the reviewers. Following review, the data DOI will be issued and included in the final version of the manuscript together with the last access date].

385

*Author contribution.* DAN performed the SABER and NAOMI data processing, O<sub>3</sub> retrieval calculations, and co-ordinated the study. PTV provided atmospheric model data (WACCM-D) for the retrievals. WDJC and MAC assembled and tested the 11.072 GHz O<sub>3</sub> spectrometer (NAOMI), deployed the instrument at Ny-Ålesund, and provided technical details. MK is a principal investigator for the Ny-Ålesund MOSAIC project and carried out instrument tests. AEER provided MOSAIC data acquisition code and instrument development support.

390

*Competing interests.* The authors declare that they have no conflict of interest.



395 *Acknowledgements.* This work has been supported in part by the UK’s Natural Environment Research Council (NERC)  
Technologies Proof-of-Concept grant reference NE/P003478/1 “Satellite TV-based Ozone and OH Observations using  
Radiometric Measurements (STO<sub>3</sub>RM)” awarded to DAN. NAOMI testing and deployment was supported by the Royal  
Society Newton Fund reference NI150103 “The Effect of High-Energy Particle Precipitation from Space on the Earth’s  
Atmosphere” awarded to MK and MAC. PTV was supported by Academy of Finland project number 335555 “ICT-Solutions  
400 to Understand Variability of Arctic Climate (ICT-SUNVAC)”. The authors thank the ARTS and Qpack development teams  
and P. Kirsch at BAS for assistance configuring and running the code. The SABER and GATS teams are acknowledged for  
making the satellite datasets available and the NASA Global Modeling and Assimilation Office for MERRA-2.

## References

- Andersson, M., Verronen, P., Rodger, C., Clilverd, M. A., and Seppälä, A.: Missing driver in the Sun–Earth connection from  
405 energetic electron precipitation impacts mesospheric ozone, *Nat. Commun.*, 5, 5197, <https://doi.org/10.1038/ncomms6197>,  
2014.
- Baker, D. N., Erickson, P. J., Fennell, J. F., Foster, J. C., Jaynes, A. N., and Verronen, P. T.: Space Weather Effects in the  
Earth’s Radiation Belts, *Space Sci. Rev.*, 214, 17, <https://doi.org/10.1007/s11214-017-0452-7>, 2018.
- Brasseur, G. P. and Solomon, S.: *Aeronomy of the Middle Atmosphere*, 3rd ed., Springer, Dordrecht, Netherlands, 2005.
- 410 Buehler, S. A., Eriksson, P., Kuhn, T., von Engeln, A., and Verdes, C.: ARTS, the atmospheric radiative transfer simulator, *J.*  
*Quant. Spectrosc. Radiat. Transfer*, 91(1), 65–93, <https://doi.org/10.1016/j.jqsrt.2004.05.051>, 2005.
- Buehler, S. A., Mendrok, J., Eriksson, P., Perrin, A., Larsson, R., and Lemke, O.: ARTS, the Atmospheric Radiative Transfer  
Simulator – version 2.2, the planetary toolbox edition, *Geosci. Model Dev.*, 11, 1537–1556, <https://doi.org/10.5194/gmd-11-1537-2018>, 2018.
- 415 Daae, M., Espy, P., Nesse Tyssøy, H., Newnham, D., Stadsnes, J., and Søråas, F.: The effect of energetic electron precipitation  
on middle mesospheric night-time ozone during and after a moderate geomagnetic storm, *Geophys. Res. Lett.*, 39, L21811,  
<https://doi.org/10.1029/2012GL053787>, 2012.
- Eriksson, P., Jiménez, C., and Buehler, S. A.: Qpack, a general tool for instrument simulation and retrieval work, *J. Quant.*  
*Spectrosc. Radiat. Transfer*, 91(1), 47–64, <https://doi.org/10.1016/j.jqsrt.2004.05.050>, 2005.
- 420 Eriksson, P., Buehler, S. A., Davis, C. P., Emde, C., and Lemke, O.: ARTS, the atmospheric radiative transfer simulator,  
version 2, *J. Quant. Spectrosc. Radiat. Transfer*, 112(10), 1551–1558, <https://doi.org/10.1016/j.jqsrt.2011.03.001>, 2011.
- Hartogh, P., Jarchow, C., Sonnemann, G. R., and Grygalashvily, M.: On the spatiotemporal behavior of ozone within the  
upper mesosphere/mesopause region under nearly polar night conditions, *J. Geophys. Res.*, 109, D18303,  
<https://doi.org/10.1029/2004JD004576>, 2004.
- 425 Hays, P. B. and Roble, R. G.: Observation of mesospheric ozone at low latitudes, *Planet. Space Sci.*, 21(2), 273–279,  
[https://doi.org/10.1016/0032-0633\(73\)90011-1](https://doi.org/10.1016/0032-0633(73)90011-1), 1973.



- Kulikov, M. Y., Nechaev, A. A., Belikov, M. V., Vorobeva, E. V., Grygalashvily, M., Sonnemann, G. R., and Feigin, A. M.: Boundary of nighttime ozone chemical equilibrium in the mesopause region from SABER data: Implications for derivation of atomic oxygen and atomic hydrogen, *Geophys. Res. Lett.*, 46, 997–1004, <https://doi.org/10.1029/2018GL080364>, 2019.
- Li, A., Roth, C. Z., Pérot, K., Christensen, O. M., Bourassa, A., Degenstein, D. A., and Murtagh, D. P.: Retrieval of daytime mesospheric ozone using OSIRIS observations of O<sub>2</sub> ( $a^1\Delta_g$ ) emission, *Atmos. Meas. Tech.*, 13, 6215–6236, <https://doi.org/10.5194/amt-13-6215-2020>, 2020.
- Limpasuvan, V., Orsolini, Y. J., Chandran, A., Garcia, R. R., and Smith, A. K.: On the composite response of the MLT to major sudden stratospheric warming events with elevated stratopause, *J. Geophys. Res. Atmos.*, 121, <https://doi.org/10.1002/2015JD024401>, 2016.
- López-Puertas, M., García-Comas, M., Funke, B., Gardini, A., Stiller, G. P., von Clarmann, T., Glatthor, N., Laeng, A., Kaufmann, M., Sofieva, V. F., Froidevaux, L., Walker, K. A., and Shiotani, M.: MIPAS observations of ozone in the middle atmosphere, *Atmos. Meas. Tech.*, 11, 2187–2212, <https://doi.org/10.5194/amt-11-2187-2018>, 2018.
- Marsh, D. R., Smith, A., Brasseur, G., Kaufmann, M., and Grossmann, K.: The existence of a tertiary ozone maximum in the high latitude middle mesosphere, *Geophys. Res. Lett.*, 28, 4531–4534, <https://doi.org/10.1029/2001GL013791>, 2001.
- Marsh, D. R., Mills, M. J., Kinnison, D. E., and Lamarque, J.-F.: Climate change from 1850 to 2005 simulated in CESM1 (WACCM), *J. Climate*, 26, 7372–7391, <https://doi.org/10.1175/JCLI-D-12-00558.1>, 2013.
- Mlynczak, M. G., et al.: Atomic oxygen in the mesosphere and lower thermosphere derived from SABER: Algorithm theoretical basis and measurement uncertainty, *J. Geophys. Res. Atmos.*, 118, 5724–5735, <https://doi.org/10.1002/jgrd.50401>, 2013.
- Mlynczak, M. G., Hunt, L. A., Russell, J. M., and Marshall, B. T.: Updated SABER night atomic oxygen and implications for SABER ozone and atomic hydrogen, *Geophys. Res. Letters*, 45, 5735–5741, <https://doi.org/10.1029/2018GL077377>, 2018.
- Newnham, D. A., Clilverd, M. A., Kosch, M., Seppälä, A., and Verronen, P. T.: Simulation study for ground-based Ku-band microwave observations of ozone and hydroxyl in the polar middle atmosphere, *Atmos. Meas. Tech.*, 12, 2, 1375–1392, <https://doi.org/10.5194/amt-12-1375-2019>, 2019.
- Newnham, D. A., Clilverd, M. A., Clark, W. D. J., Kosch, M., Verronen, P. T., and Rogers, A. E. E.: Processed ozone (O<sub>3</sub>) vertical profiles from NAOMI and SABER observations during 2017–2020, Polar Data Centre, Natural Environment Research Council, UK, <https://doi.org/10.xxxx/xxxx>, 2021. [Authors' note: Datasets are available for the reviewers. Following review, the data DOI will be issued and included in the final version of the manuscript].
- Palmroth, M., Grandin, M., Sarris, T., Doornbos, E., Tourgaidis, S., Aikio, A., Buchert, S., Clilverd, M. A., Dandouras, I., Heelis, R., Hoffmann, A., Ivchenko, N., Kervalishvili, G., Knudsen, D. J., Kotova, A., Liu, H.-L., Malaspina, D. M., March, G., Marchaudon, A., Marghitu, O., Matsuo, T., Miloch, W. J., Moretto-Jørgensen, T., Mpaloukidis, D., Olsen, N., Papadakis, K., Pfaff, R., Pirnaris, P., Siemes, C., Stolle, C., Suni, J., van den IJssel, J., Verronen, P. T., Visser, P., and Yamauchi, M.: Lower-thermosphere–ionosphere (LTI) quantities: current status of measuring techniques and models, *Ann. Geophys.*, 39, 189–237, <https://doi.org/10.5194/angeo-39-189-2021>, 2021.



- Pancheva, D., Mukhtarov, P., and Smith, A. K.: Nonmigrating tidal variability in the SABER/TIMED mesospheric ozone, *Geophys. Res. Lett.*, 41, 4059–4067, <https://doi.org/10.1002/2014GL059844>, 2014.
- Rodgers, C. D.: Inverse methods for atmospheric sounding: Theory and Practice, vol. 2 of Series on Atmospheric, Ocean and Planetary Physics, World Scientific, <https://doi.org/10.1142/3171>, 2000.
- 465 Rogers, A. E. E., Lekberg, M., and Pratap, P.: Seasonal and diurnal variations of ozone near the mesopause from observations of the 11.072-GHz line, *J. Atmos. Oceanic Technol.*, 26, 2192–2199, <https://doi.org/10.1175/2009JTECHA1291.1>, 2009.
- Rogers, A. E. E., Erickson, P., Fish, V. L., Kittredge, J., Danford, S., Marr, J. M., Arndt, M. B., Sarabia, J., Costa, D., and May, S. K.: Repeatability of the seasonal variations of ozone near the mesopause from observations of the 11.072-GHz line, *J. Atmos. Oceanic Technol.*, 29, 1492–1504, <https://doi.org/10.1175/JTECH-D-11-00193.1>, 2012.
- 470 Ryan, N. J. and Walker, K. A.: The effect of spectroscopic parameter inaccuracies on ground-based millimeter wave remote sensing of the atmosphere, *J. Quant. Spectrosc. Radiat. Transfer*, 161, 50–59, <https://doi.org/10.1016/j.jqsrt.2015.03.012>, 2015.
- Ryan, N. J., Walker, K. A., Raffalski, U., Kivi, R., Gross, J., and Manney, G. L.: Ozone profiles above Kiruna from two ground-based radiometers, *Atmos. Meas. Tech.*, 9, 4503–4519, <https://doi.org/10.5194/amt-9-4503-2016>, 2016.
- 475 Sinnhuber, M., Nieder, H., and Wieters, N.: Energetic Particle Precipitation and the Chemistry of the Mesosphere/Lower Thermosphere, *Surv. Geophys.*, 33, 1281–1334, <https://doi.org/10.1007/s10712-012-9201-3>, 2012.
- Siskind, D. E., Merkel, A. W., Marsh, D. R., Randall, C. E., Hervig, M. E., Mlynczak, M. G., and Russell, J. M.: Understanding the effects of polar mesospheric clouds on the environment of the upper mesosphere and lower thermosphere, *J. Geophys. Res. Atmos.*, 123, 11,705–11,719, <https://doi.org/10.1029/2018JD028830>, 2018.
- 480 Smith, A. K., Harvey, V. L., Mlynczak, M. G., Funke, B., García-Comas, M., Hervig, M., Kaufmann, M., Kyrölä, E., López-Puertas, M., McDade, I., Randall, C. E., Russell III, J. M., Sheese, P. E., Shiotani, M., Skinner, W. R., Suzuki, M., and Walker, K. A.: Satellite observations of ozone in the upper mesosphere, *J. Geophys. Res. Atmos.*, 118, 5803–5821, <https://doi.org/10.1002/jgrd.50445>, 2013.
- Smith, A. K., M. López-Puertas, B. Funke, M. García-Comas, M. G. Mlynczak, and L. A. Holt: Nighttime ozone variability  
485 in the high latitude winter mesosphere, *J. Geophys. Res. Atmos.*, 119, 13,547–13,564, <https://doi.org/10.1002/2014JD021987>, 2015.
- Smith, A. K., Espy, P. J., López-Puertas, M., and Tweedy, O. V.: Spatial and temporal structure of the tertiary ozone maximum in the polar winter mesosphere. *J. Geophys. Res. Atmos.*, 123, 4373–4389, <https://doi.org/10.1029/2017JD028030>, 2018.
- Smith-Johnsen, C., Orsolini, Y., Stordal, F., Limpasuvan, V., and Pérot, K.: Nighttime mesospheric ozone enhancements  
490 during the 2002 southern hemispheric major stratospheric warming, *J. Atmos. Sol.-Terr. Phys.*, 168, 100–108, [doi.org/10.1016/j.jastp.2017.12.018](https://doi.org/10.1016/j.jastp.2017.12.018), 2018.
- Sofieva, V. F., Kyrölä, E., Verronen, P. T., Seppälä, A., Tamminen, J., Marsh, D. R., Smith, A. K., Bertaux, J.-L., Hauchecorne, A., Dalaudier, F., Fussen, D., Vanhellemont, F., Fanton d’Andon, O., Barrot, G., Guirlet, M., Fehr, T., and Saavedra, L.:



- 495 Spatio-temporal observations of the tertiary ozone maximum, *Atmos. Chem. Phys.*, 9, 4439–4445,  
<https://doi.org/10.5194/acp-9-4439-2009>, 2009.
- Tenneti, S. N. and Rogers, A. E. E.: Development of an optimized antenna and other enhancements of a spectrometer for the study of ozone in the mesosphere, VSRT and MOSAIC Memo 063, available at: [https://www.haystack.mit.edu/wp-content/uploads/2020/07/memo\\_VSRT\\_063.pdf](https://www.haystack.mit.edu/wp-content/uploads/2020/07/memo_VSRT_063.pdf) (last access: 21 February 2019), 2009.
- 500 Verronen, P. T., and R. Lehmann: Enhancement of odd nitrogen modifies mesospheric ozone chemistry during polar winter, *Geophys. Res. Lett.*, 42, <https://doi.org/10.1002/2015GL066703>, 2015.
- Verronen, P. T., Andersson, M. E., Marsh, D. R., Kovács, T., and Plane, J. M. C.: WACCM-D – Whole Atmosphere Community Climate Model with D-region ion chemistry, *J. Adv. Model. Earth Sy.*, 8, 954–975, <https://doi.org/10.1002/2015MS000592>, 2016.
- 505 Zawedde, A. E., Nesse Tyssøy, H., Stadsnes, J., and Sandanger, M. I.: Are EEP events important for the tertiary ozone maximum?, *J. Geophys. Res. Space Phys.*, 124, 5976–5994, <https://doi.org/10.1029/2018JA026201>, 2019.